Circuit Modeling Methodology for UWB Omnidirectional Small Antennas

Stanley B. T. Wang, *Student Member, IEEE,* Ali M. Niknejad, *Member, IEEE,* and Robert W. Brodersen, *Fellow, IEEE*

Manuscript received _____

Affiliation of authors

Department of Electrical Engineering and Computer Sciences
University of California, Berkeley
Berkeley, CA 94720-1770
U.S.A.

Correspondence Address

Stanley Wang
Berkeley Wireless Research Center
2108 Allston Way, Suite 200
Berkeley, CA 94704-1302
U.S.A.

Voice: (510) 666-3194
Fax: (510) 883-0270
E-mail: sbtwang@eecs.berkeley.edu

Circuit Modeling Methodology for UWB Omnidirectional Small Antennas

Stanley B. T. Wang, *Student Member, IEEE,* Ali M. Niknejad, *Member, IEEE,* and Robert W. Brodersen, *Fellow, IEEE*

Abstract – In Ultra-wideband (UWB) systems, antennas act as filters that introduce a frequency dependent response from the transmitter to receiver. To capture the waveform dispersion so that one can equalize/compensate at the transmitter/receiver, a new circuit modeling methodology that handles omnidirectional small antennas is proposed. By transforming the antennas into the degenerated Foster canonical forms and utilizing the waveform-omnidirectional property, it is shown that the transmitted electric field waveform is a scaled version of the voltage across the radiation resistor in the model. Extended Thevenin/Norton equivalent circuits with dependent sources tracking the frequency dependence of the antenna effective length are also built for receiving antennas. Simulation and experimental results show that this methodology is effective over a wide bandwidth and suitable for modeling most existing UWB antennas.

Index Terms – Ultra-wideband, small antenna, equivalent circuit, Foster canonical form, antenna transfer function.

I. INTRODUCTION

In 2002, the FCC released the use of Ultra-wideband (UWB) transmission in several frequency bands (0-960MHz, 3.1-10.6GHz, and 22-29GHz) with an Effective Isotropic Radiated Power (EIRP) below -41.3dBm/MHz [1]. On one hand, the large bandwidth enables short-range high data-rate communication [2] and high resolution positioning [3], which are infeasible in narrowband systems; on the other hand, utilization of the large bandwidth imposes new design challenges in UWB systems.

One of the challenges is the design of UWB antennas. It is required that a UWB antenna possess broad impedance bandwidth, high radiation efficiency, small size, omnidirectional radiation pattern (small directivity) and broad radiation pattern bandwidth (or frequency-independent radiation pattern). These properties are generally strong functions of the antenna electrical size. For antennas that are electrically small, the impedance match is poor due to the high quality factor but the radiation pattern is almost constant with frequency; for antennas operating close to the first resonant frequency, the impedance match is good and the radiation pattern is a weak function of frequency; for antennas operating well above the first resonant frequency, the impedance match is good but the radiation pattern changes rapidly with frequency. UWB antenna design is thus about shaping the antenna around the first resonant frequency to achieve simultaneous impedance matching and constant radiation pattern over a wide bandwidth. The state-of-the-art UWB antennas report up to 4:1 impedance bandwidth but less than 3:1 bandwidth meeting both impedance and radiation pattern requirements [4-6].

Another challenge is the design of UWB antenna/circuit interface. In traditional narrowband systems, all the design parameters are expressed in single values, i.e. power, gain, reflection coefficient, etc., and the received power can easily be calculated by putting these numbers into Friis transmission formula. Antennas are modeled as resistors with a standard value, say 50Ω, when designing the interface circuits at the operating frequency. The phase responses of the antennas and RF front-end circuits are negligible since it is also a constant and can be embedded into the channel response and compensated at the receiver. However, in UWB systems, not only are the parameters frequency-dependent, complicating the analysis, but also the whole transmitter-to-

receiver transfer function needs to be constructed in order to take into account the waveform dispersion caused by the antennas [7]. The Friis transmission formula is no longer capable of delivering this information for UWB design, and a new methodology needed.

A common way of determining the frequency and angle dependent transfer functions is to directly measure or simulate the two-port S-parameters of the transmitting/receiving antenna pair [8-9]. Poles and residues can be extracted from S-parameters to analytically express the transfer function [10]. To make it complete, attempts have been made to simultaneously model the antenna input impedance and transfer function [11], but only the input impedance is modeled by circuit elements while the transfer function is not, which makes it difficult to use for circuit designers. Some software is available for EM/circuit co-simulation, but the simulation is time-consuming. In this paper, it will be shown that at the transmitter as long as the antennas operate below a frequency where there is no angular dependency on the radiated waveforms, the input impedance and transfer function are correlated and both of them can be modeled by simple circuit networks. Receiving antenna model can also be built using Thevenin and Norton equivalent circuits.

This paper is organized as follows. Section II first presents the modeling technique for omnidirectional small transmitting antennas, and then examples on a small dipole antenna, a Large Current Radiator, and a circular dipole antenna will be given. Following that, Section III covers modeling techniques for omnidirectional small receiving antennas. In Section IV, experimental results for monopole antenna pairs are presented to show the effectiveness of the model.

II. Modeling Omnidirectional Small Transmitting Antennas

Generally, antennas are linear, passive elements that their input impedances can be represented by Foster canonical forms, as shown in Fig. 1, which follows assuming no ohmic loss [12]. The first Foster canonical form (Fig. 1(a)) is suitable for modeling “electric antennas” which are electrically open at DC. The second Foster canonical form (Fig. 1(b)) is for modeling “magnetic antennas” which are electrically short at DC. For

example, dipole and monopole antennas are electric antennas while loop antennas are magnetic antennas. The RLC tanks in the figures model the resonances of an antenna when the operating frequency increases. For UWB antennas of interest, one operates the antennas in the regime that their radiation pattern is constant with frequency, i.e. below the 2nd resonant frequency, so the Foster canonical forms can be degenerated to that shown in Fig. 2. The circuit topology in Fig. 2(a) has been successfully employed to model the input impedance of dipole antennas [13]. Note that since there is only one resistor in each circuit in Fig. 2, all the power radiated from the antenna is equal to the power dissipated on the resistor, that is [14],

$$\frac{V_{rad}\,(t-\frac{r}{c})^2}{R_{rad}} = r^2 \oint_{4\pi} \frac{E(\theta,\phi,r,t)^2}{\eta_0} d\varpi \qquad \textbf{Eq. 1}$$

where c is the speed of light, r is the observation distance from the antenna, ϖ is the solid angle, η_0 is the free-space characteristic impedance that is 377Ω, and $E(\theta,\phi,r,t)$ is the far-zone E-field propagating in the direction (θ,ϕ). The circuit models can be thought of as a load resistor R_{rad} with a passive LC bandpass filter in the front.

Another property of small antennas is that they are mostly *waveform-omnidirectional*, i.e. the waveforms of the radiated E-fields propagating in all directions are the same, and differ only in magnitude. This property is formulated as [14]

$$E(\theta,\phi,r,t) = \alpha(\theta,\phi) \times E(\theta_o,\phi_o,r,t) \qquad \textbf{Eq. 2}$$

where $\alpha(\theta,\phi)$ is a direction-dependent scaling factor. By combining Eq. 1 and Eq. 2, we obtain

$$\frac{V_{rad}(t-\frac{r}{c})^2}{R_{rad}} = r^2 \oint_{4\pi} \alpha(\theta,\phi)^2 d\varpi \times \frac{E(\theta_o,\phi_o,r,t)^2}{\eta_0} = \beta r^2 \frac{E(\theta_o,\phi_o,r,t)^2}{\eta_0} \qquad \textbf{Eq. 3}$$

where β is a constant, and

$$E(\theta,\phi,r,t) = \pm\frac{1}{r}\sqrt{\frac{\eta_0}{\beta R_{rad}}}\alpha(\theta,\phi)V_{rad}(t-\frac{r}{c}) = \gamma(\theta,\phi,r)V_{rad}(t-\frac{r}{c}) \qquad \textbf{Eq. 4}$$

Therefore, once the constant $\gamma(\theta,\phi)$ is calculated, one can scale the time-domain voltage V_{rad} across the radiation resistor R_{rad} in the circuit models shown in Fig. 2 and derive waveforms of the radiated E-fields in any direction. In other words, the transfer function information from an antenna input voltage/current to far-zone E-fields are embedded in its input impedance as long as the antenna is *waveform-omnidirectional*.

A. Modeling a Small Dipole Antenna

We first verify the model by considering the simplest antenna – electrically small dipole. Assume the current phasor $I(z)$ on a dipole antenna (Fig. 3) is [14-15]

$$I(z) = I_m \sin k(h - |z|) \qquad \textbf{Eq. 5}$$

Due to symmetry on the horizontal plane, the far-zone E-field does not depend on the azimuthal angle ϕ and thus

$$E(\theta,\phi) = E_\theta = \eta_0 H_\phi = j\frac{I_m \eta_0 k \sin\theta}{2\pi r} e^{-jkr} \int_0^h \sin k(h-z)\cos(kz\cos\theta)dz = \frac{j60I_m}{r} e^{-jkr} F(\theta) \qquad \textbf{Eq. 6}$$

where k is wave number and $F(\theta)$ is the pattern function. When $kh << 1$

$$F(\theta) = \frac{\cos(kh\cos\theta) - \cos kh}{\sin\theta} \cong \frac{1 - \frac{1}{2}(kh\cos\theta)^2 - (1 - \frac{1}{2}(kh)^2)}{\sin\theta} = \frac{1}{2}(kh)^2 \sin\theta$$

and yields

$$E_\theta = \frac{j30I_m}{r} e^{-jkr} (kh)^2 \sin\theta = E_{\theta=90^o} \sin\theta \qquad \textbf{Eq. 7}$$

Eq. 7 shows that when the operating frequency is low, the far-zone E-fields differ from that radiating to $\theta = 90^o$ by a scaling factor $\sin\theta$. Therefore, a small dipole antenna is *waveform-omnidirectional*.

Fig. 4 shows the FDTD EM simulation [16] results of a 6cm dipole antenna gain from 0-5GHz over the elevation angles. It can be seen that as long as the frequency is below 1GHz (h=0.1λ) the magnitude responses only differ by a scaling factor (Fig. 4(a)). After normalization (Fig. 4(b)), the magnitude responses overlap exactly at low frequency region, and the error is less than 0.3dB as frequency goes up to 1GHz, and increases to

about 3dB at 2.5GHz which is the first resonant frequency. Phase responses also match well (Fig. 4(c)), hence verifying the *waveform-omnidirectionality* of small dipoles.

By fitting the input impedance of the circuit in Fig. 2(a) to that of the 6cm dipole antenna from FDTD simulation using an optimization tool, we obtain C1 = 0.68pF, L1 = 1.24nH, C2 = 0.64pF, L2 = 4.91nH and R_{rad} = 187Ω. The resulting impedances from SPICE and FDTD simulations are shown in Fig. 5. Both the real and imaginary parts of the impedances match very well up to 5GHz, which is almost twice the first resonant frequency. Fig. 6 and Fig. 7 show two sets of time-domain simulation results. Fig. 6(a) shows a 0.6ns-wide Gaussian voltage waveform with most of its power concentrated below 2GHz. This waveform is sent into the antenna through a 50Ω resistor, and the voltage waveform V_{rad} and the far-zone E-field at $\theta = 90^o$ at 1m away from the antenna are derived in SPICE and FDTD respectively. After scaling and time shifting, Fig. 6(b) shows that the two normalized waveforms match well. The ratio of V_{rad} to $E_\theta = 90^o$ at 1m before normalization is 2.2 (meter). From Eq. 1, 3, and 6, β is derived and the theoretical ratio of V_{rad} to $E_\theta = 90^o$ at 1m is 2.0 (meter), which is within 10% of the simulation results. Similarly, a Gaussian-modulated sinusoidal waveform shown in Fig. 7(a) with -10dB bandwidth from 1.7-2.5GHz is sent into the antenna and the resulting waveforms are shown in Fig. 7(b). Again, the waveforms from SPICE and FDTD match well. It shows that the model is valid at least up to the antenna's first resonant frequency.

One can also get some insights of the antenna behavior from the circuit model. According to the model developed above, when the frequency is low, the transfer function is approximated as

$$\frac{E(\theta,\phi,r)}{V_s} = \frac{E(\theta,\phi,r)}{V_{in}} \bullet \frac{V_{in}}{V_s} \cong \frac{1}{r}\sqrt{\frac{\eta_0}{R_{rad}}}\sqrt{\frac{3}{8\pi}} s^2 L_2 C_1 \frac{sC_1}{sC_1R_s + 1} \qquad \textbf{Eq. 8}$$

It can be seen that there are two parts involved in the transfer function: one is the impedance division from source voltage V_s to antenna input V_{in}; the other is from the antenna input V_{in} to far-zone E-field. When the source resistance R_s is small, say 50Ω as in above cases, the transfer function follows a second-derivative (second-order high-pass) behavioral relation and is consistent with other UWB antenna analyses on small dipoles

[17]. However, when R_s increases, the transfer function will gradually changes and the relation eventually becomes closer to first-derivative (first-order high-pass). This means that although the antenna transfer function is fixed, one can still tweak the overall transfer function by setting different impedance value of the driver stage. It is also possible to come up with an equalizer to compensate the filtering effect of the antenna and eliminate the waveform dispersion.

When the operating frequency increases up to the resonant frequency, the reactive parts in the model act as a matching network that transforms radiation resistance R_{rad} to antenna input resistance R_{in}. The transfer function thus becomes

$$\frac{E(\theta,\phi,r)}{V_s} \cong \frac{1}{r}\sqrt{\frac{\eta_0}{R_{in}}}\sqrt{\frac{3}{8\pi}}\frac{R_{in}}{R_s + R_{in}} \qquad \textbf{Eq. 9}$$

Note that there is no frequency dependent term in the equation, so a non-dispersive radiation is achieved near the resonant frequency.

B. Modeling a Large Current Radiator

The Large-Current Radiator (LCR) has been proposed as a UWB antenna [3, 17] and a version of it is shown in Fig. 8. FDTD simulation shows that the resonant frequency of the LCR is around 2GHz. Since it is a magnetic antenna, the circuit model in Fig. 2(b) is utilized. After curve-fitting the input impedance of the circuit model to that of the LCR, component values are derived as L1 = 49.4nH, L2 = 1.65nH, C2 = 0.13pF, Rrad = 31Ω. Note that C1 is ignored since we limit the operating frequency to be below 1GHz. Driving the antenna by a step function shown in Fig. 9(a) with a source resistance equal to 1Ω, the normalized waveforms of V_{rad} from SPICE and E_{rad} at $\theta = 0^o$ from FDTD are derived and shown in Fig. 9(b). Again, the agreement between the waveforms validates the model. The small glitches on the E_{rad} waveform are due to FDTD simulation error. The ratio of V_{rad} and Erad is 0.153 (meter).

Similar to small dipoles, the input voltage to far-zone E-field transfer function can be formulated for electrically small magnetic antennas

$$\frac{E(\theta,\phi,r)}{V_{in}} \cong \frac{1}{r}\sqrt{\frac{\eta_0}{R_{rad}}}\sqrt{\frac{3}{8\pi}}\,\frac{sL_1}{sL_1+R_s}\,sC_2R_{rad} \qquad \textbf{Eq. 10}$$

When the source resistance R_s is small, the transfer function follows a first-derivative relation (first-order high-pass). When R_s is large, the transfer function becomes a second-derivative relation (second-order high-pass).

C. Modeling a Circular Dipole Antenna

To show that this methodology is not limited to simple electrically small antennas, we also model a circular dipole antenna [18] that has been used in the 3-10GHz range. The antenna geometry is shown in Fig. 10. From FDTD simulation, this antenna self-resonates (imaginary part of impedance crosses zero) at 4.3GHz, and its -10dB impedance bandwidth is from 3.6GHz to over 10GHz. It is *waveform-omnidirectional* (phase responses overlap and magnitude responses diverge by 3dB) up to ~7GHz. Because it is an electric antenna, the circuit network from Fig. 2(a) is used. After fitting the input impedance, the circuit component values are derived as C1=0.58pF, L1=0.85nH, C2=0.53pF, L2=1.5nH and Rrad=81Ω. Fig. 11 and Fig. 12 show the simulation results for the antenna driven by a Gaussian and Gaussian–derivative waveforms respectively. In the first case, input signal -10dB bandwidth is from DC to 5.5GHz that is 28% larger than its self-resonant frequency (Fig. 11(a)). The radiated E-field at $\theta = 90^o$ matches the normalized V_{rad} well (Fig. 11(b)) and the ratio of V_{rad} and E_{rad} is 1.61 (meter). In the second case, input signal -10dB bandwidth is from 2 to 11GHz (Fig. 12(a)). The high frequency corner is over twice the self-resonant frequency. It can be seen in Fig. 12(b) that the normalized V_{rad} still makes a reasonable prediction of the far-zone E-fields, and behaves like a weighted average of the radiated E-fields at $\theta = 90^o$ and $\theta = 40^o$. It is closer to the E-field at $\theta = 90^o$ because more power is radiated in that direction.

From the above cases, it is found that the degenerated Foster canonical forms in Fig. 2 are capable of modeling an antenna's input impedance way above the first resonant frequency, thus the operating bandwidth of the transmitting antenna model is mainly constrained by the *waveform-omnidirectionality* that is one of the specifications of good

UWB antennas. Therefore, this modeling technique is applicable to most state-of-the-art UWB antennas.

III. Modeling Omnidirectional Small Receiving Antennas

In general, a receiving antenna can be modeled as a Thevenin equivalent circuit (Fig. 13) with source impedance equal to the antenna impedance and open circuit voltage equal to the incident electric field scaled by a frequency dependent complex factor, i.e. the effective length $\overline{L}_{eff}$ [12, 15, 20]. Not only for the receiver, the effective length is also a parameter that relates the radiated E-field and the input current when the antenna is transmitting [20, 21]:

$$\overline{E} = -j\omega \frac{\mu_0}{4\pi} \frac{e^{-j\beta r}}{r} \overline{L}_{eff} I_{in} . \qquad \textbf{Eq. 11}$$

Considering omnidirectional small electric antennas that can be modeled as Fig. 2(a), if one reformulates Eq. 4 in frequency domain and express V_{rad} as a function of I_{in}:

$$\overline{E} = -\frac{e^{-j\beta r}}{r} \sqrt{\frac{\eta_0}{\beta R_{rad}}} \alpha(\theta,\phi) Z_2 I_{in} , \qquad \textbf{Eq. 12}$$

where Z_2 represents the impedance of the parallel tank with C2, L2, and Rrad in Fig. 2(a). Equating Eq. 11 and Eq. 12 shows that

$$\overline{L}_{eff} = \frac{\sqrt{\frac{\eta_0}{\beta R_{rad}}} \alpha(\theta,\phi) Z_2}{j\omega \frac{\mu_0}{4\pi}} . \qquad \textbf{Eq. 13}$$

Eq. 13 demonstrates that the information of the effective length of an omni-directional small antenna is embedded in the values of C2, L2, and Rrad. When the frequency is low, Z_2 is dominated by $j\omega L2$ and $\overline{L}_{eff}$ becomes a frequency independent constant, matching the simple equivalent circuit proposed for electrically small antennas in [19]. When the frequency increases, the change of Z_2 contributed by C2 and Rrad reflects the non-

uniformity of the induced currents on the antenna and results in $\overline{L}_{eff}$'s deviation from a real value. Theoretically, the valid operating frequency range of this improved receiving antenna model is the same as that of the corresponding transmitting model, which is beyond the first resonant frequency.

Same analogy can be applied to omnidirectional small magnetic antennas as modeled in Fig. 2(b):

$$\overline{L}_{eff} = \frac{\sqrt{\frac{\eta_0}{\beta R_{rad}}}\alpha(\theta,\phi)R_{rad}\frac{Z_1}{Z_1+Z_2}}{j\omega\frac{\mu_0}{4\pi}}, \qquad \textbf{Eq. 14}$$

where Z_1 represents the impedance of the parallel tank with L1 and C1 and Z_2 represents that of the series tank with L2, C2 and Rrad. If we transform the network to its Norton equivalent (Fig. 13(b)),

$$\overline{L}_{eff}' = \frac{\overline{L}_{eff}}{Z_{ant}} = \frac{\sqrt{\frac{\eta_0}{\beta R_{rad}}}\alpha(\theta,\phi)R_{rad}}{j\omega\frac{\mu_0}{4\pi}Z_2}. \qquad \textbf{Eq. 15}$$

When the frequency is low, Z_2 is dominated by $1/j\omega C2$, and $\overline{L}_{eff}'$ again becomes a real constant, matching the result in [19].

According to the Thevenin equivalent circuit for electric antennas, when the antenna is electrically small, $\overline{L}_{eff}$ is a real constant (L_{eff}) and its impedance is dominated by the capacitor C1, and the output voltage of the antenna is

$$V_L = \frac{Z_{ckt}}{Z_{ant}+Z_{ckt}}V_{oc} = \frac{Z_{ckt}}{Z_{ant}+Z_{ckt}}L_{eff}E_{in} = \frac{sC_1Z_{ckt}}{1+sC_1Z_{ckt}}L_{eff}E_{in}. \qquad \textbf{Eq. 16}$$

Therefore, when the receiver circuit load is a small resistance, the transfer function from the incident E-field to the output voltage follows a first-derivative relation (first-order high-pass). When the load impedance is large compared to C1, it approaches a linear

relation without dispersion. Waveform dispersion may also be eliminated by adopting a capacitive load.

On the other hand, for an electrically small magnetic antenna, its admittance is dominated by the inductor L1, and from the Norton equivalent circuit, the output current of the antenna is

$$I_L = \frac{Y_{ckt}}{Y_{ant}+Y_{ckt}} I_{sc} = \frac{Y_{ckt}}{Y_{ant}+Y_{ckt}} L_{eff}\,'E_{in} = \frac{sL_1Y_{ckt}}{1+sL_1Y_{ckt}} L_{eff}\,'E_{in}. \qquad \textbf{Eq. 17}$$

By the same analogy, when the receiver circuit load is a large resistance, the transfer function from the incident H-field to the output current follows a first-derivative relation (first-order high-pass). When the load impedance is small compared to L1, it approaches a linear relation without dispersion. Waveform dispersion may also be eliminated by adopting an inductive load.

Although the UWB waveform can be preserved by picking the right circuit loading based on either a small electric antenna or small magnetic antenna being chosen, it is far from ideal in terms of power transfer because the impedances are not matched. The ohmic loss of the antenna, thus far ignored, may also lead to a large noise figure of the antenna and severely degrades the receiver performance.

If the frequency is increased to its first resonance and assumes L_{eff} does not deviate from a real constant too much, the transfer function is

$$V_L = \frac{Z_{ckt}}{Z_{ant}+Z_{ckt}} V_{oc} = \frac{R_{ckt}}{R_{ant}+R_{ckt}} L_{eff} E_{in}. \qquad \textbf{Eq. 18}$$

Hence, similar to the case in transmitter, operating the receiving antenna near the first resonant frequency enables the possibility of simultaneous power-match and non-dispersive signal reception, which is the optimal approach to take.

The complete transmitting-receiving antenna circuit model for omnidirectional small electric antennas is shown in Fig. 14. Two voltage-controlled voltage sources and a current-controlled current source are utilized to fulfill the transfer function including the impedance ratio in $\overline{L_{eff}}$ expression. The transimpedance Z_{21} can be written as

$$Z_{21} = \frac{1}{r} Z_{2t} \sqrt{\frac{\eta_0}{\beta R_{rad1}}} \sqrt{\frac{\eta_0}{\beta R_{rad2}}} \alpha_1(\theta,\phi)\alpha_2(\theta,\phi) \frac{Z_{2r}}{j\omega \frac{\mu_0}{4\pi}}. \quad \textbf{Eq. 19}$$

If the transmitting and receiving antennas are swapped, the reversed transimpedance Z_{12} can be derived as

$$Z_{12} = \frac{1}{r} Z_{2r} \sqrt{\frac{\eta_0}{\beta R_{rad2}}} \sqrt{\frac{\eta_0}{\beta R_{rad1}}} \alpha_2(\theta,\phi)\alpha_1(\theta,\phi) \frac{Z_{2t}}{j\omega \frac{\mu_0}{4\pi}}. \quad \textbf{Eq. 20}$$

From Eq. 19 and Eq. 20 it can been seen that $Z_{21} = Z_{12}$, which means reciprocity holds in the model.

Simple modification can be applied to get alternative circuit models for omni-directional small magnetic antennas.

IV. Measurement Results of Monopole Antennas

In order to demonstrate the effectiveness of the modeling methodology, monopole antennas with various lengths (1.5cm, 2.5cm, and 3.5cm) are paired up for line-of-sight transmission and the two-port S-parameters were measured with an HP8719 network analyzer. A metal plate with dimension 1.1m by 0.5m is employed as the ground plane, which isolates the measurement equipments underneath and reduces interference and multipath effects. The experiment was taken in a spacious room with walls far away from the setup. The distance between the two antennas is 1.05m, which introduces 3.5ns of delay from the transmitter to receiver. One-port S-parameters of the three monopoles are first taken to obtain the antenna impedances. Model parameters are then derived by curve fitting. As shown in Fig. 15, a nice fit between the models and measurement results are achieved from 50MHz to 5GHz for the 1.5cm and 2.5cm monopoles and from 50MHz to 4GHz for the 3.5cm monopole, which implies that the circuit model is able to match the antenna impedances beyond the 2nd resonant frequency. With the assumption that the radiation pattern of the monopole antennas follows a sinusoidal function as in Eq. 7, $\alpha(\theta,\phi)$ in Eq. 2-4 can be calculated. Two-port S-parameters can then be predicted using the antenna models shown in Fig. 14 and compared to that from measurements.

Fig. 16 shows the S_{21} (same as S_{12}) data between two 1.5cm monopole antennas from measurement and our prediction. Both the magnitude and phase responses match well up to 6GHz — accurate beyond the first resonant frequency. The magnitude response peaks at the first resonant frequency due to better match to 50Ω. The discrepancies that occur at low frequency region are believed to result from interference and the lack of sensitivity of the instrument.

The same procedure is taken in between the 2.5cm and 3.5cm monopoles and the results are shown in Fig. 17. Two models are built to predict the transfer function. One is that the 2.5cm monopole transmits while the 3.5cm monopole receives; the other is the 3.5cm monopole transmits while the 2.5cm monopole receives. As predicted in the previous section, due to reciprocity, the two simulated frequency responses overlap exactly, and both of them match well with the experimental results up to 6GHz, which is beyond the antennas' 2nd resonant frequencies.

V. CONCLUSION

A circuit modeling methodology for UWB omnidirectional small antennas on both transmitting and receiving sides has been proposed and verified by simulations and measurements. It is able to model the antenna/circuit interface and the corresponding transfer functions by circuit simulators and dramatically save the computing time. It has also been shown that not only the antenna itself may introduce dispersion, varying the interface circuit impedance may also lead to different levels of wave shaping, which can be predicted by this model. It is therefore possible to do waveform design by choosing non-standard driver impedance. Operating the antenna close to the first resonant frequency is still the optimal approach in terms of power match and non-dispersive transmission.

ACKNOWLEDGMENT

The authors thank Ian O'Donnell and Mike Chen at BWRC, Robert Fleming and Cherie Kushner at Aether Wire & Location, Inc., and Prof. Daniel Schaubert and Prof.

David Pozar at the University of Massachusetts for their valuable suggestions. The authors are also grateful to Prof. Tzyh-Ghuang Ma at NTUST in Taiwan for the valuable discussion and help on improving the manuscript. Assistance from Yuen-Hui Chee during the measurement is appreciated.

This work was supported by the Army Research Office grant #065861, Intel Corp., and the industrial members of BWRC.

REFERENCES

[1] FCC Notice of Proposed Rule Making, "Revision of Part 15 of the commission's rules regarding ultra-wideband transmission systems," ET-Docket 98-153.

[2] IEEE 802.15.3a task group website. http://www.ieee802.org/15/pub/TG3a.html

[3] R. Fleming and C. Kushner, "Integrated Ultra-wideband localizers," *1999 UWB Conference*, Sept. 1999. Available: http://www.aetherwire.com

[4] S. Suh, W. Stutzman, W. Davis, A. Waltho and J. Schiffer, "A novel CPW-fed disc antenna," in *IEEE AP-S Int. Symp. Dig.*, vol. 3, Monterey, CA, June 2004, pp. 2919-2922.

[5] T. G. Ma and S. K. Jeng, "Planar miniature tapered-slot-fed annular slot antennas for ultra-wideband radios," to appear in *IEEE Trans. Antennas Propagat.*, Vol. 53, Mar. 2005.

[6] H. G. Schantz, "Bottom fed planar elliptical UWB antennas," *in Proc. IEEE Conf. Ultra Wideband Systems and Technologies*, pp. 219-223, Nov. 2003.

[7] Z. N. Chen, X. H. Wu, N. Yang and M. Y. W. Chia, "Considerations for source pulses and antennas in UWB radio systems," *IEEE Trans. Antennas Propagat.*, vol. 52, pp. 1739-1748, July 2004.

[8] S. Licul and W. A. Davis, "Ultra-wideband (UWB) antenna measurements using vector network analyzer," in *IEEE AP-S Int. Symp. Dig.*, vol. 2, Monterey, CA, June 2004, pp. 1319-1322.

[9] X. Qing and Z. N. Chen, "Transfer functions measurement for UWB antennas," in *IEEE AP-S Int. Symp. Dig.*, vol. 3, Monterey, CA, June 2004, pp. 2532-2535.

[10] S. Licul and W. A. Davis, "Pole/residue modeling of UWB antenna systems," in *IEEE AP-S Int. Symp. Dig.*, vol. 2, Monterey, CA, June 2004, pp. 1748-1751.

[11] I. Pele, A. Chousseaud and S. Toutain, "Simultaneous modeling of impedance and radiation pattern antenna for UWB pulse modulation," in *IEEE AP-S Int. Symp. Dig.*, vol. 2, Monterey, CA, June 2004, pp. 1871-1874.

[12] S. Ramo, J. R. Whinnery and T. Van Duzer, *Fields and waves in communication electronics*, John Wiley & Sons, 1994.

[13] M. Hamid and R. Hamid, "Equivalent circuit of dipole antenna of arbitrary length," *IEEE Trans. on Antennas Propagat.*, vol. 45, pp. 1695-1696, Nov. 1997.

[14] S. B. Wang, A. M. Niknejad and R. W. Brodersen, "Modeling omnidirectional small antennas for UWB applications," in *IEEE AP-S Int. Symp. Dig.*, vol. 2, Monterey, CA, June 2004, pp. 1295-1298.

[15] D. Cheng, *Field and wave electromagnetics*, Addison Wesley, 1989.

[16] Remcom XFDTD v5.1.

[17] J. Taylor, "Introduction to Ultra-wideband radar systems," CRC Press, 1995.

[18] H. G. Schantz, "Planar elliptical element Ultra-wideband dipole antennas," in *IEEE AP-S Int. Symp. Dig.*, vol. 3, June 2002, pp. 16-21.

[19] C. Baum, "Parameters for some electrically-small electromagnetic sensors," *Sensor and Simulations Notes*, Air Force Weapons Laboratory, March 1967.

[20] C. Balanis, *Antenna theory: analysis and design*, 2nd edition, John Wiley & Sons, 1997.

[21] R. Meys, "A summary of the transmitting and receiving properties of antennas," *IEEE Antennas and Propagation Magazine*, vol. 42, no. 3, pp. 49-53, June 2000.

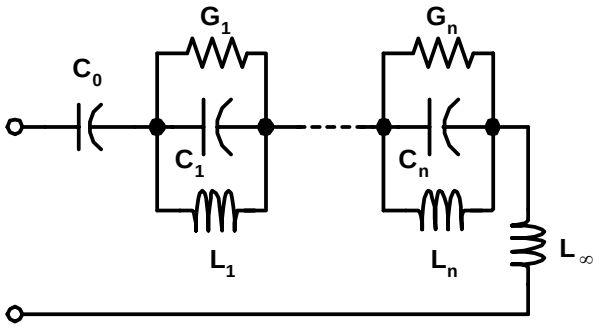

(a)

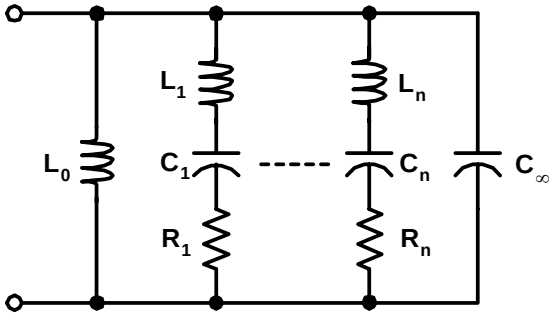

(b)

Figure 1. Foster canonical forms for (a) electric antennas and (b) magnetic antennas.

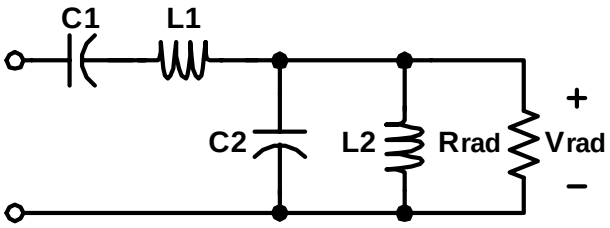

(a)

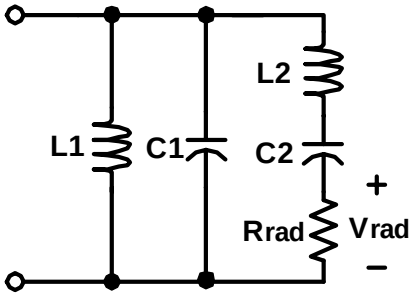

(b)

Figure 2. Degenerated Foster canonical forms for (a) electric antennas and (b) magnetic antennas.

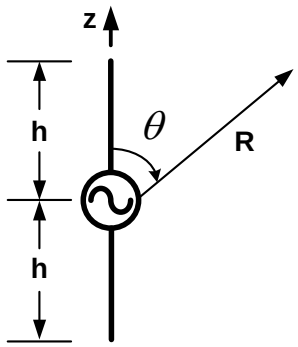

Figure 3. Illustration of a small dipole antenna.

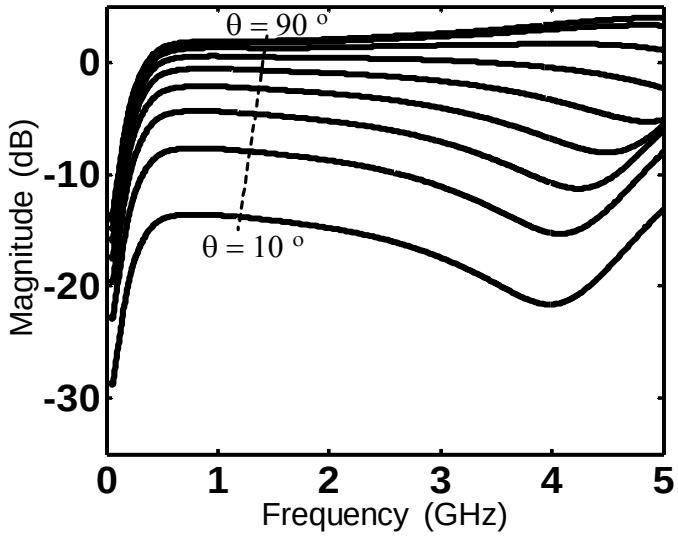

(a)

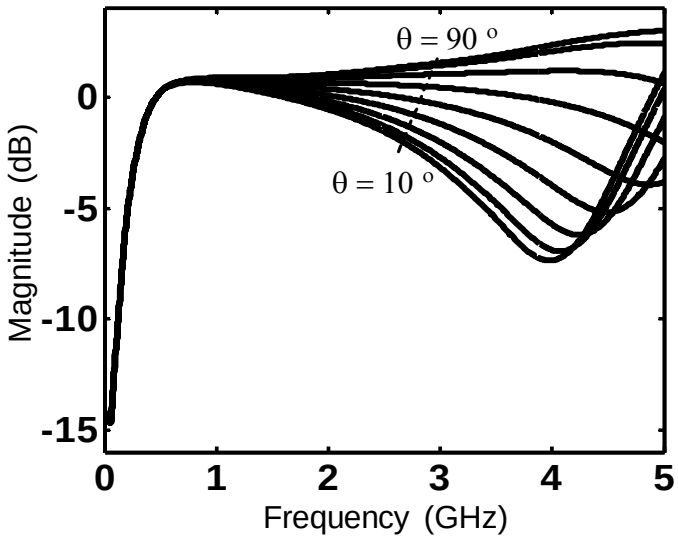

(b)

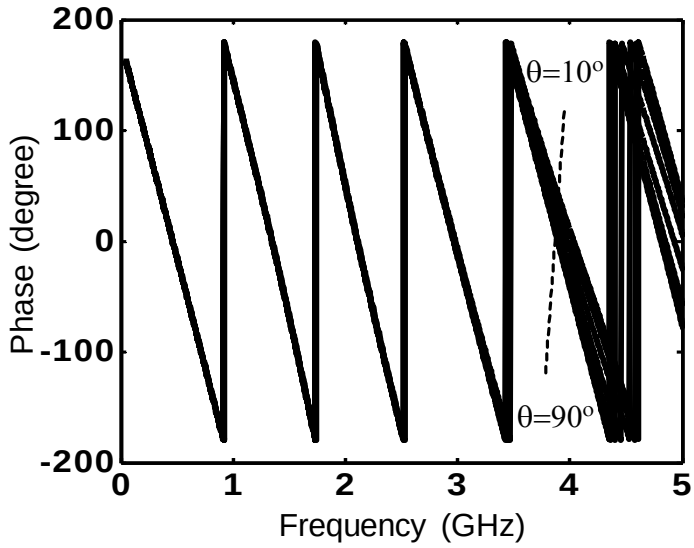

(c)

Figure 4. Transfer function from the 6cm dipole antenna input to far-zone E-fields. (a) Magnitude response. (b) Normalized magnitude response. (c) Phase response.

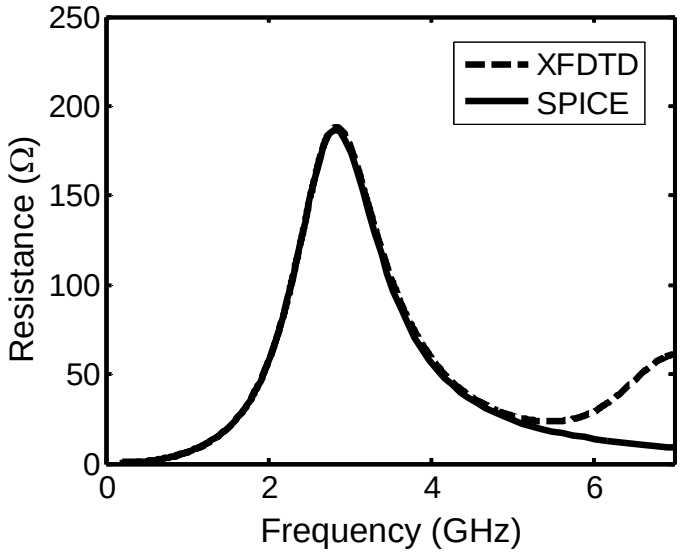

(a)

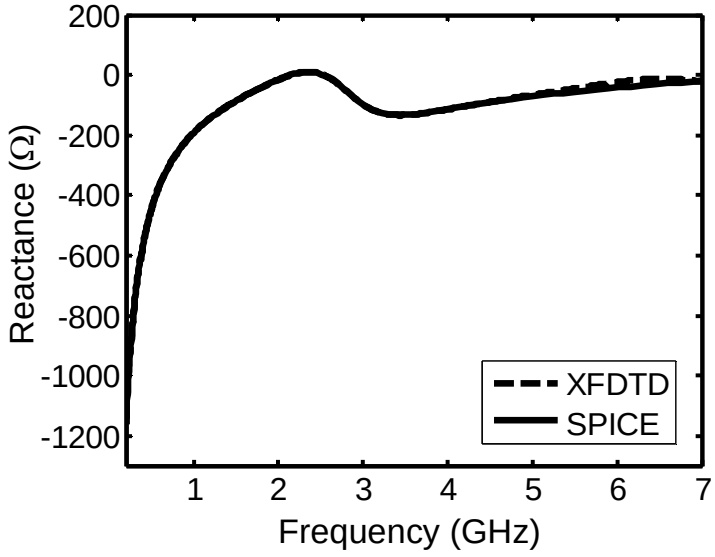

(b)

Figure 5. (a) Real and (b) imaginary parts of input impedance of the 6cm dipole antenna.

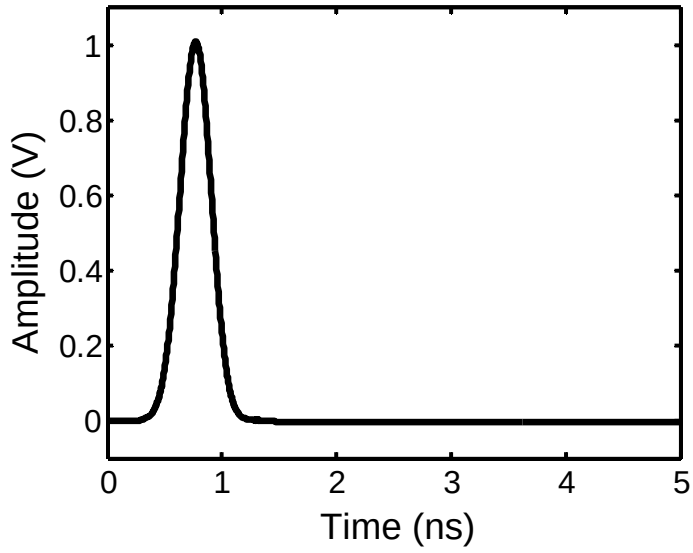

(a)

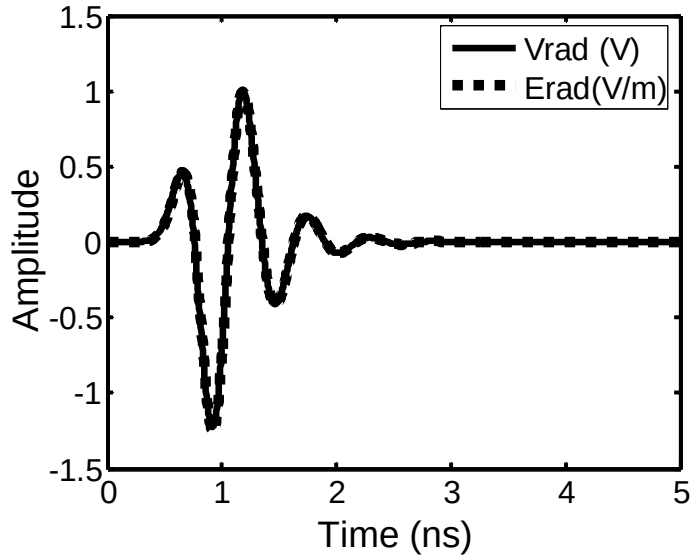

(b)

Figure 6. Time-domain waveforms of the 6cm dipole antenna. (a) shows the signal source waveform and (b) shows the normalized voltage waveform across Rrad from SPICE and normalized radiated E-field in $\theta = 90^{o}$ from XFDTD. The input source resistance is 50Ω and the -10dB bandwidth of the input signal is DC-2GHz.

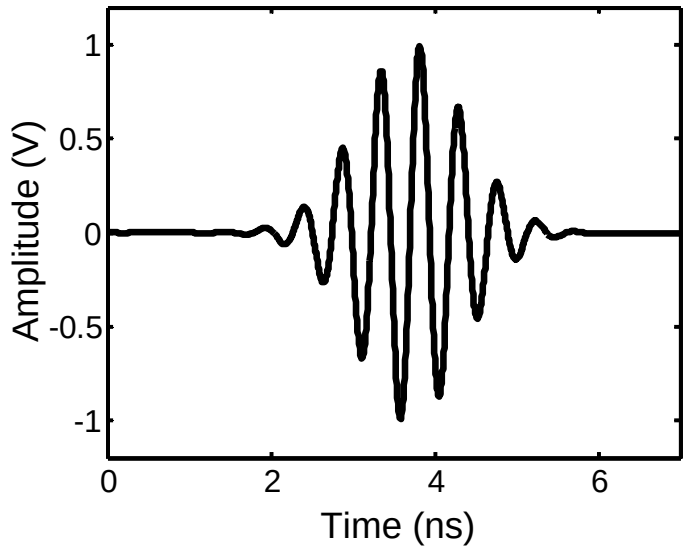

(a)

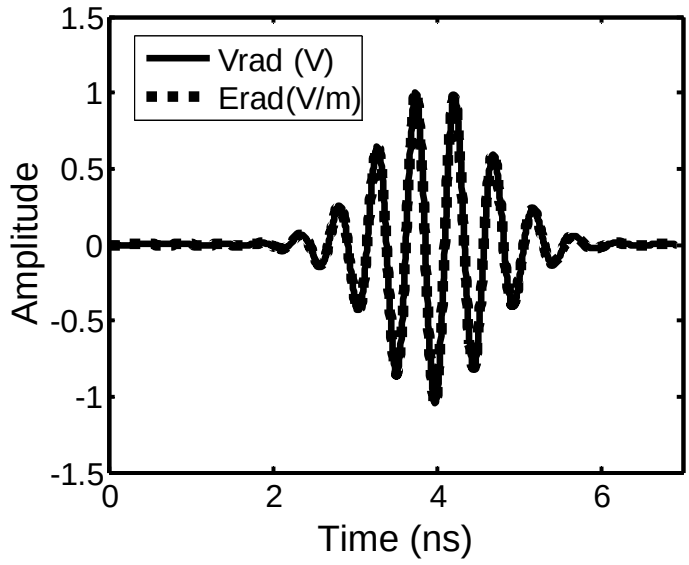

(b)

Figure 7. Time-domain waveforms of the 6cm dipole antenna. (a) shows the signal source waveform and (b) shows the normalized voltage waveform across Rrad from SPICE and normalized radiated E-field in $\theta = 90^{o}$ from XFDTD. The input source resistance is 50Ω and the -10dB bandwidth of the input signal is 1.7-2.5GHz.

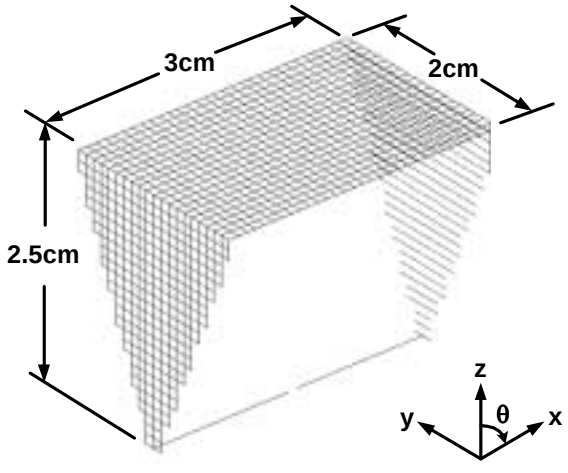

Figure 8. Large-Current Radiator (LCR).

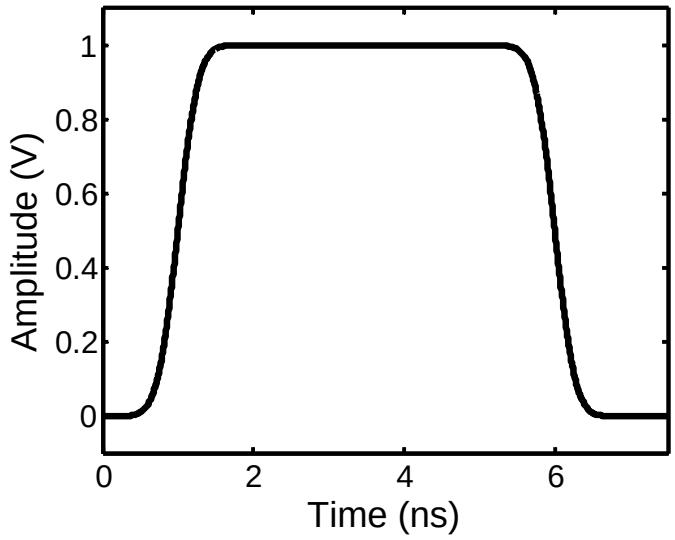

(a)

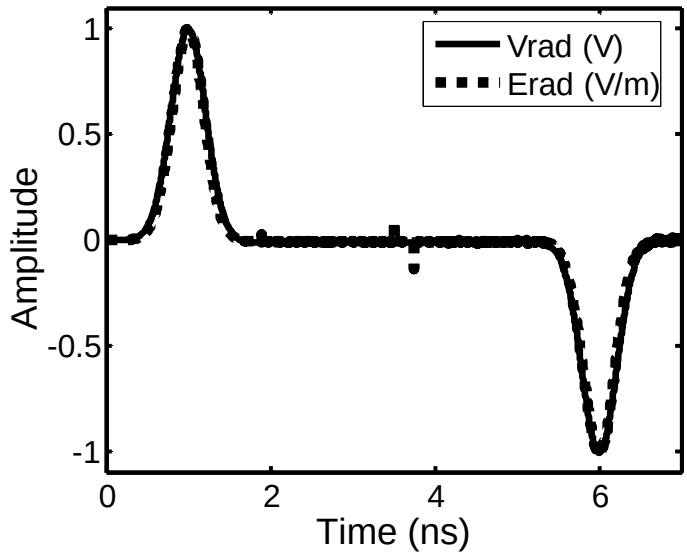

(b)

Figure 9. Time-domain waveforms of the LCR. (a) shows the signal source waveform and (b) shows the normalized voltage waveform across Rrad from SPICE and normalized radiated E-field in $\theta = 90^{o}$ from XFDTD. The input source resistance is 1Ω and the -10dB bandwidth of the input signal is DC-1GHz.

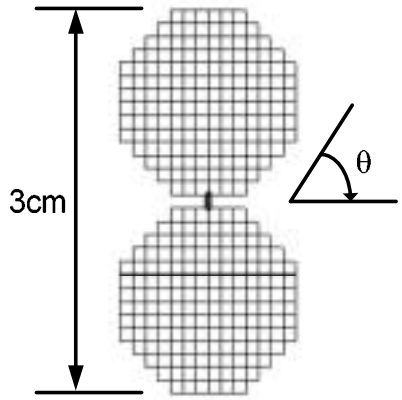

Figure 10. A 3cm circular dipole antenna.

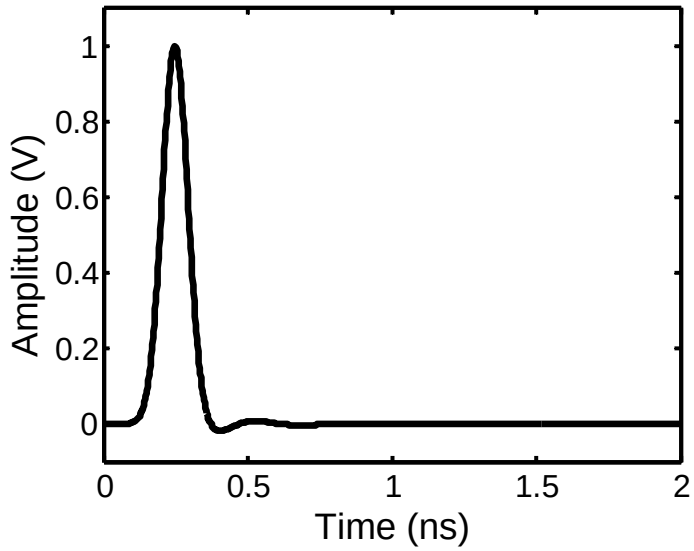

(a)

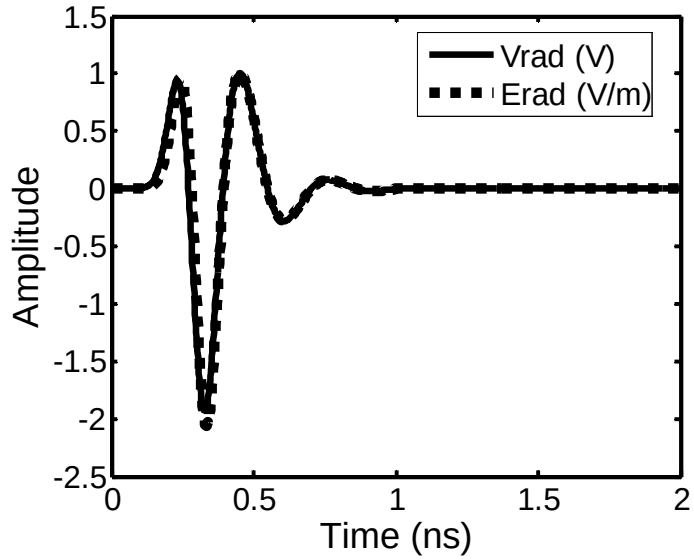

(b)

Figure 11. Time-domain waveforms of the 3cm circular dipole antenna. (a) shows the signal source waveform and (b) shows the normalized voltage waveform across Rrad from SPICE and normalized radiated E-field in $\theta = 90^{o}$ from XFDTD. The input source resistance is 50Ω and the -10dB bandwidth of the input signal is DC-5.5GHz.

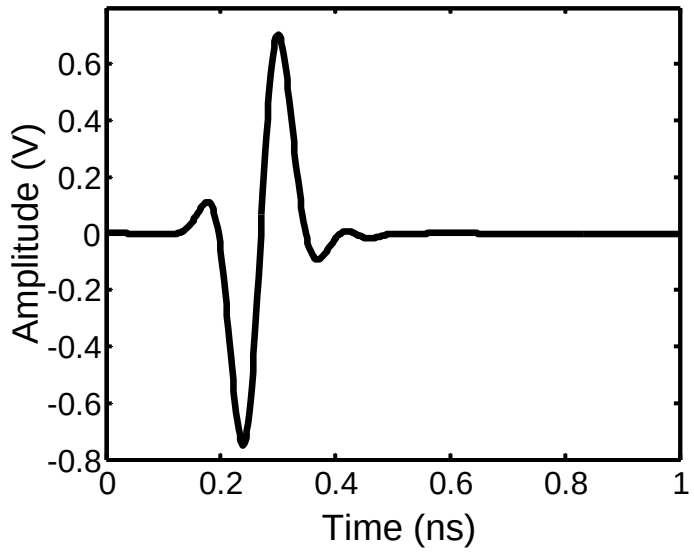

(a)

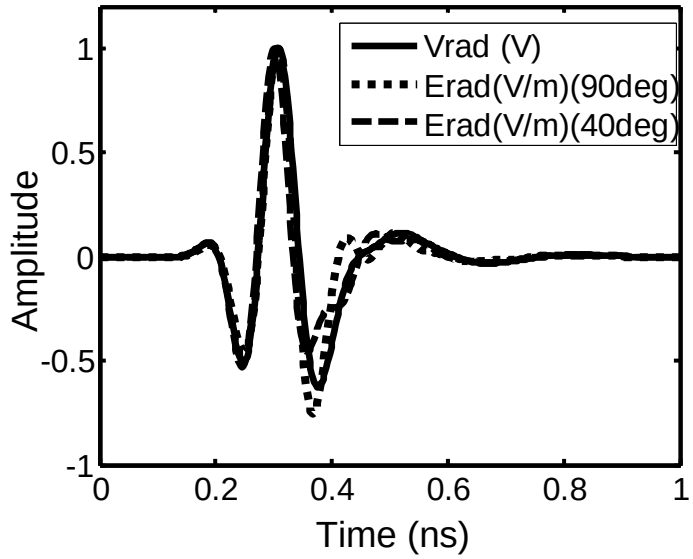

(b)

Figure 12. Time-domain waveforms of the 3cm circular dipole antenna. (a) shows the signal source waveform and (b) shows the normalized voltage waveform across Rrad from SPICE and normalized radiated E-field in $\theta = 90^{o}$ from XFDTD. The input source resistance is 50Ω and the -10dB bandwidth of the input signal is 2-11GHz.

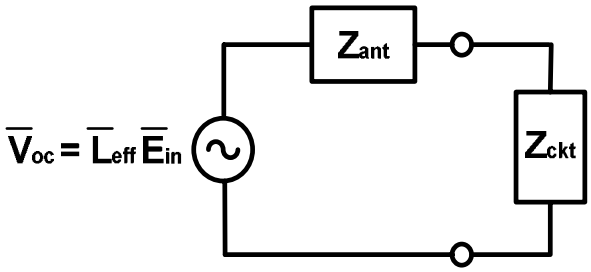

(a)

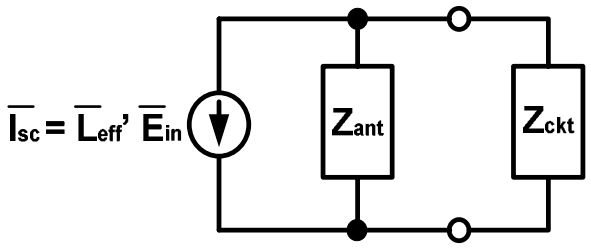

(b)

Figure 13. (a) Thevenin and (b) Norton equivalents for receiving antennas.

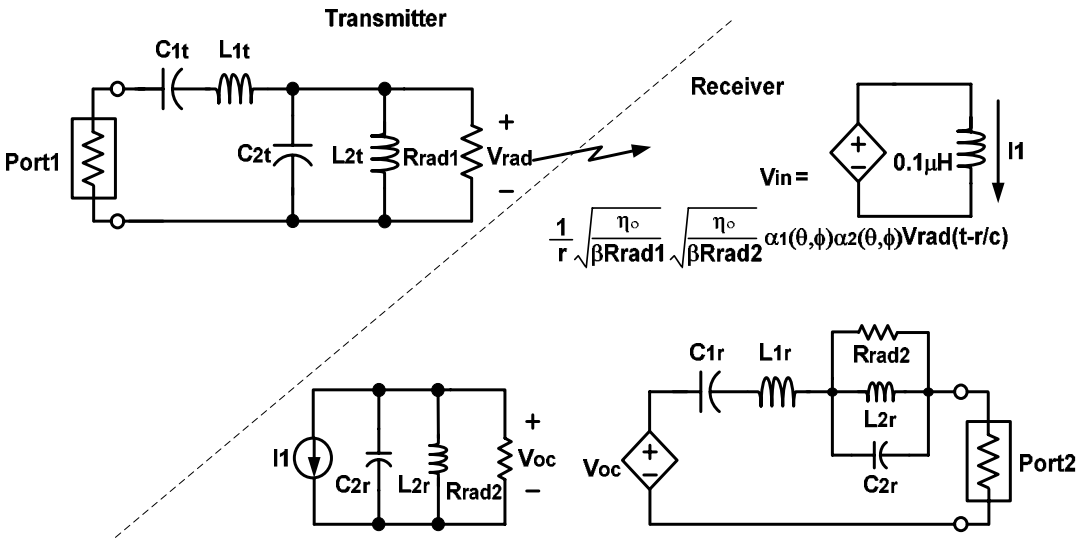

Figure 14. The complete transmitter-to-receiver antenna model for omni-directional small electric antennas.

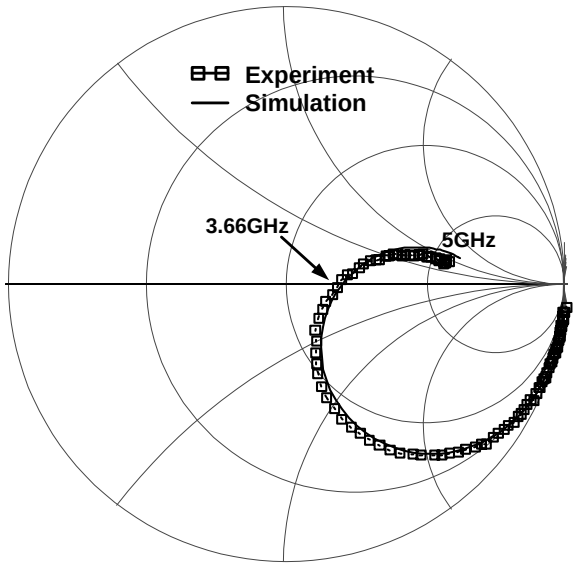

(a)

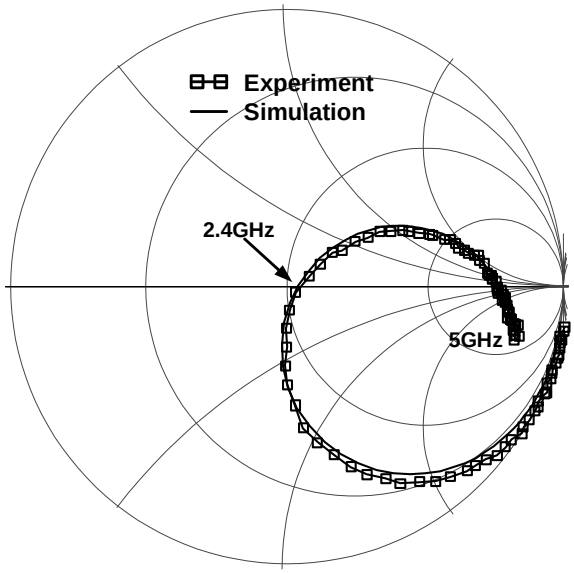

(b)

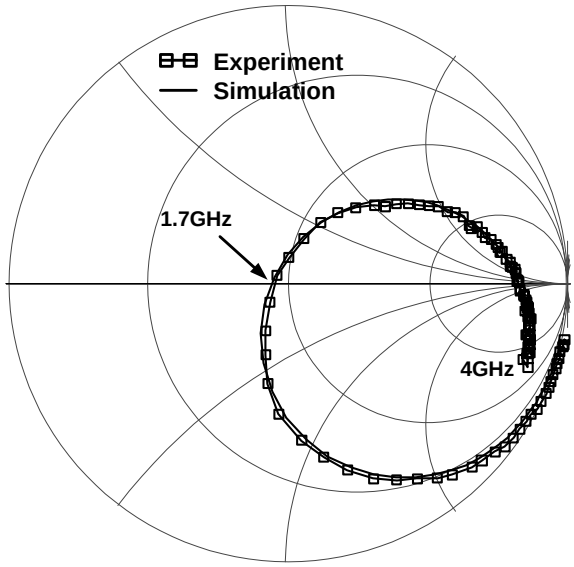

(c)

Figure 15. Measured and simulated input impedances of (a) 1.5cm monopole, (b) 2.5cm monopole, and (c) 3.5cm monopole.

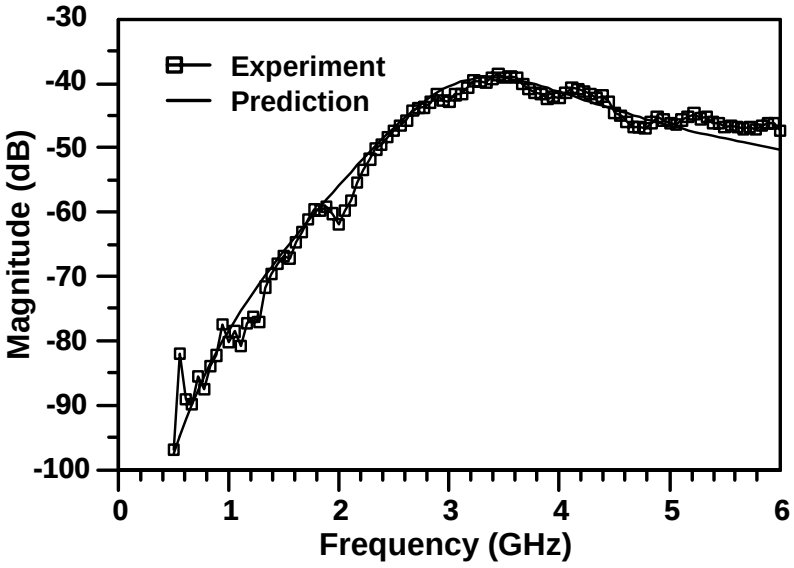

(a)

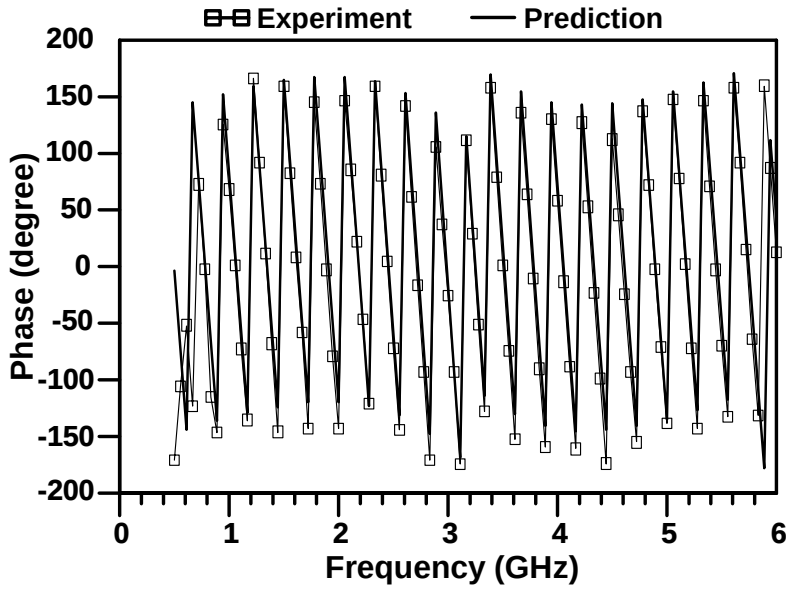

(b)

Figure 16. Measured and predicted/simulated S-parameters of a 1.5cm monopole antenna pair. (a) Magnitude response of S_{21}. (b) Phase response of S_{21}.

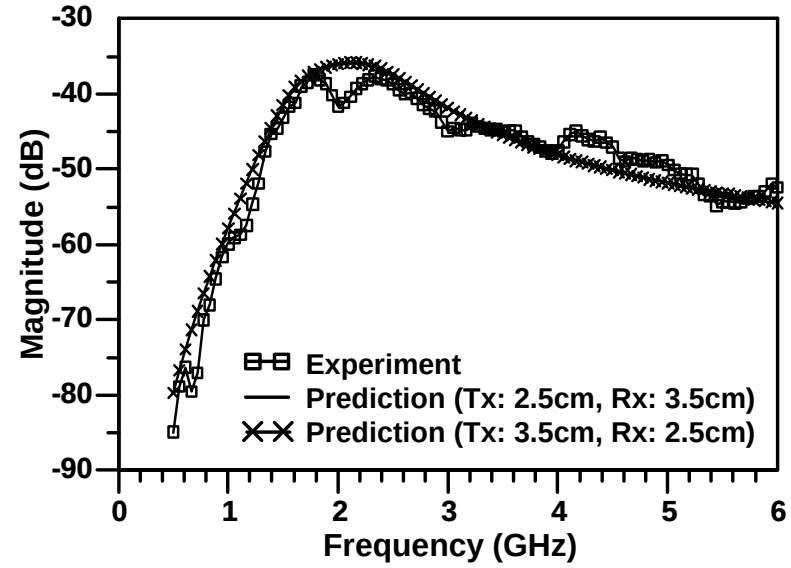

(a)

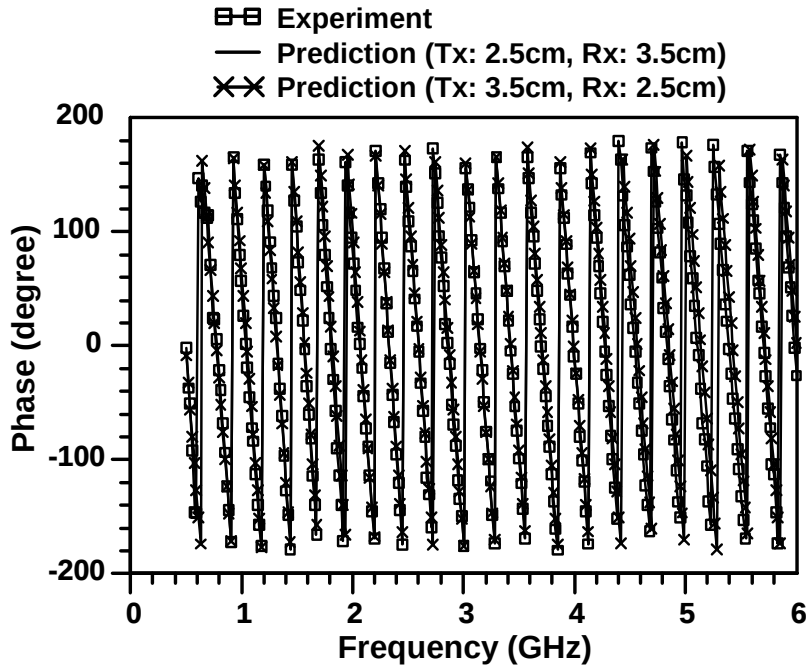

(b)

Figure 17. Measured and predicted/simulated S-parameters of a 2.5cm/3.5cm monopole antenna pair. (a) Magnitude response of S_{21}. (b) Phase response of S_{21}.